Interaction with the Extratropics as a New Hypothesis for the Spectral Peak of the Madden–Julian Oscillation

PAUL E. ROUNDY[a] AND CRIZZIA MIELLE DE CASTRO[a]

[a] *University at Albany, State University of New York, Albany, New York*

(Manuscript received 23 October 2023, in final form 5 February 2024, accepted 9 March 2024)

ABSTRACT: The Madden–Julian oscillation (MJO) propagates eastward as a disturbance of mostly zonal wind and precipitation along the equator. The initial diagnosis of the MJO spectral peak at 40–50-day periods suggests a reduction in amplitude associated with slower MJO events that occur at lower frequencies. If events on the low-frequency side of the spectral peak continued to grow in amplitude with reduced phase speed, the spectrum would just be red. Wavelet regression analysis of slow and fast eastward-propagating MJO signals during northern winter assesses how associated moisture and wind patterns could explain why slow MJO events achieve lower amplitude in tracers of moist convection. Results suggest that slow MJO events favor a ridge anomaly over Europe, which drives cool dry air equatorward over Africa and Arabia as the active convection develops over the Indian Ocean. We hypothesize that dry air tracing back to this source, together with a longer duration of the events, leads to associated convection diminishing along the equator and instead concentrating in the Rossby gyres off the equator.

SIGNIFICANCE STATEMENT: The Madden–Julian oscillation (MJO) dominates the subseasonal variability of the tropical atmosphere. This work suggests that it favors maximum convective activity in the 40–50-day period range because lower-frequency MJO signals tend to import more cool dry air from the extratropics and along the equator, thereby weakening the slower events.

KEYWORDS: Intraseasonal variability; Subseasonal variability; Tropical variability

1. Introduction

Explanations of the dominant mechanisms of the Madden–Julian oscillation (MJO; Madden and Julian 1972) have resisted consensus for decades. Just like the MJO, eastward-moving disturbances of zonal wind and rainfall in the tropics also characterize convectively coupled Kelvin waves. Both demonstrate dominant zonal winds in phase with geopotential height anomalies in the upper troposphere (Roundy 2020). However, several lines of evidence suggest a physical distinction between the MJO and Kelvin waves. First, Kelvin waves propagate eastward at phase speeds near 10–20 m s^{-1}, much faster than the MJO at phase speeds of 2–8 m s^{-1} (Wheeler and Kiladis 1999; Roundy and Frank 2004). Second, non-Kelvin features associated with the MJO include Rossby gyres in response to the MJO's convection and low pressure. The MJO's surface low pressure extends westward from the easterly winds east of the convection into westerlies collocated with the convection (Sobel and Kim 2012; Roundy 2012). Third, the two signals may occupy different regions in the wavenumber–frequency domain, as some results suggest distinct spectral peaks (Wheeler and Kiladis 1999; Hendon and Wheeler 2008).

However, on the first point, Kelvin waves themselves occur across a broad range of phase speeds (Roundy 2008), the limits of which are not objectively established. On the second point, similar non-Kelvin features as Rossby gyres also appear in convectively coupled Kelvin waves (Roundy 2008, 2012), with stronger non-Kelvin features typically occurring in waves associated with heavier rainfall. Finally, on the third point, evidence shows that intermediate disturbances fill the "spectral gap" between traditional spectral peaks of Kelvin waves and the MJO, implying that the two categories form a continuum (Roundy 2020).

Roundy (2020) showed that the intermediate signals are not merely transitional forms between the two extremes because they occur over the central Indian basin, not just the central Pacific Ocean. Events within the central Indian basin express intermediate phase speeds over extended periods of the disturbances' lifetime. The same analysis established structural consistency between the MJO spectral peak and upper-tropospheric circulation disturbances across the continuum with Kelvin waves near the equator. These disturbances exhibit eastward flow in an equatorial ridge, westward flow in an equatorial trough, dominance of zonal wind, and mass divergence east of the trough leading to eastward propagation. Rossby ridges overlap with the Kelvin wave troughs near and west of the convection and achieve their greatest amplitude well off the equator. The Kelvin wave–like eastward-moving disturbances show increasing amplitude of associated convection co-occurring with reduced phase speed from 30 to 4–5 m s^{-1} (Roundy 2012, 2020).

The upper-tropospheric outflow from convection coupled with the MJO and moist Kelvin waves generates Rossby gyres in the tropics, accelerates the subtropical jet stream, and further generates Rossby waves that propagate around the world

Denotes content that is immediately available upon publication as open access.

Corresponding author: Paul E. Roundy, proundy@albany.edu

DOI: 10.1175/JAS-D-23-0196.1

(Takasuka et al. 2021; Tulich and Kiladis 2021). These response signals occur during fast or slow disturbances, but intensity increases with stronger associated convection. Outflow from convection feeds mass in every direction from its near-equatorial center of action, including westward. However, an equatorial Kelvin wave trough anomaly maintains west of the deep convection in the upper troposphere from the fastest moist waves down in frequency to the center of the MJO spectral peak (Roundy 2020), thereby preserving the Kelvin wave identity even in the MJO. The slowest events show stronger gyre circulations relative to Kelvin waves even though they coincide with weaker convection (Roundy 2021). Yet, if the upper-tropospheric circulation merely responds to the convection driven from below, the region west of the convection would form Rossby ridges as in the Gill (1980) solution, with no Kelvin wave trough signal. Instead, the convection drives the Rossby ridges poleward of the Kelvin wave trough without filling the trough. The equatorial trough itself cannot be a direct response to convection to its east.

The Dynamics of the MJO (DYNAMO) project diagnosed upper-tropospheric Kelvin waves as the leading precursors to the development of new MJO convection over the Indian Ocean (Powell and Houze 2015). The approaching Kelvin wave–like disturbance from the west reduces deep tropospheric temperature and convective inhibition at the top of the boundary layer, thereby developing new subseasonal convective anomalies. Thus, the dynamics lead the convection, and the upper-tropospheric Kelvin wave trough anomaly persists despite the convection.

Although previously described as a dry Kelvin wave originating from the convective MJO warm pool (Sobel and Kim 2012; Milliff and Madden 1996), the upper-tropospheric MJO signal over the Western Hemisphere actually includes several different wave types. These features speed up considerably as they move from the Eastern Hemisphere to the Western Hemisphere, where MJO-associated signals move eastward from 5 to 30 m s^{-1} depending on their category. The dry Kelvin wave component of the MJO circulation propagates fast, followed by moist Kelvin waves and then by eastward advected Rossby waves (Roundy 2014; Sakaeda and Roundy 2015). As this mix of upper-tropospheric waves approaches the northern winter transition point from Western Hemisphere tropical background westerlies to Eastern Hemisphere easterlies near Africa, the eastward advected Rossby waves halt and break, while Kelvin waves filter through. Thus, contrary to popular belief, the MJO-associated upper-tropospheric circulation signal over the Indian Ocean behaves more Kelvin wave–like than the Western Hemisphere circulation of the MJO (Sakaeda and Roundy 2015).

On the other hand, the release of latent heat by convection leads to responses in the lower troposphere that overwhelm any Kelvin wave structure. Accordingly, the trough in equatorial MJO easterlies east of the convection extends westward into the lower-tropospheric westerly wind region beneath the deep convection (Yang and Wang 2019). A pure Kelvin wave signal would have included a ridge in the westerly anomalies. These factors together suggest that the equatorial MJO circulation pattern maintains a Kelvin wave–like structure in the upper troposphere, while the direct effects of convection drive lower-tropospheric circulation. Thus, we consider that a planetary-scale Kelvin wave dominates the upper-tropospheric circulation signal associated with the MJO. Unfortunately, for the argument, a moist Kelvin wave propagates at phase speeds between 10 and 20 m s^{-1}, while the MJO convection and upper-tropospheric circulation signal moves eastward at around 2–8 m s^{-1}.

Roundy (2022) demonstrated that advection by the background wind slows the eastward advance of the upper-tropospheric circulation signal associated with the MJO over the Indian Ocean, with the greatest effect at the slowest phase speeds. This result confirmed previous correlation-based conclusions by Chen and Wang (2020) and Suematsu and Miura (2022). After removing the effects of advection to find the associated speed in a resting basic state, the results showed that the upper-tropospheric circulation signal of the MJO moves eastward at 12–16 m s^{-1}, with the slowest signals being the same as those near the spectral peak in rainfall. This conforms with the MJO upper-tropospheric flow pattern behaving as a moist coupled Kelvin wave. The slowest Earth-relative MJO signals below the spectral peak possess lower-intensity convection and associate with the strongest upper-tropospheric easterly background wind. After adjusting for advection, the slowest MJO events would actually be faster in a resting basic state than the ones that occur around the center of the spectral peak. Thus, we pose the question of why the slowest Earth-relative MJO signals tend to associate with weaker convective signals. Understanding this point could explain why we observe a spectral peak in the first place because if the slower signals instead continued to amplify, the spectrum would just be red, with no peak in the 40–50-day period range.

This paper uses observations and reanalysis data to extend the wavelet analysis of Roundy (2021) and introduces a new hypothesis why planetary-scale Kelvin waves of MJO events achieve lower amplitude in metrics of deep convection at their slowest observed phase speeds.

2. Data and methods

Daily mean zonal and meridional wind, temperature, and specific humidity data at 850 hPa and geopotential height data and winds at 200 hPa, all on 1° × 1° grids from 1979 to 2020, were obtained from the ERA5 reanalysis (Hersbach et al. 2023). The NOAA ESRL provided interpolated satellite outgoing longwave radiation (OLR) data on a 2.5° × 2.5° grid (Liebmann and Smith 1996). These data were padded through February 2023 by including NOAA uninterpolated OLR data with missing data filled by using the mean anomaly of all immediate nonmissing neighbors in time and space. To obtain anomalies, linear regression following Roundy (2020) removed the long-term mean and the annual cycle with its first four harmonics.

This study modifies the space–time wavelet analysis presented by Roundy (2021) by creating base point indices for regression of MJO-associated structures moving at 2 and 7 m s^{-1} to compare slow and fast MJO signals. Roundy (2021) previously analyzed the structures of northern winter MJO signals at integer phase speeds from 1 to 8 m s^{-1}. This paper selects two cases

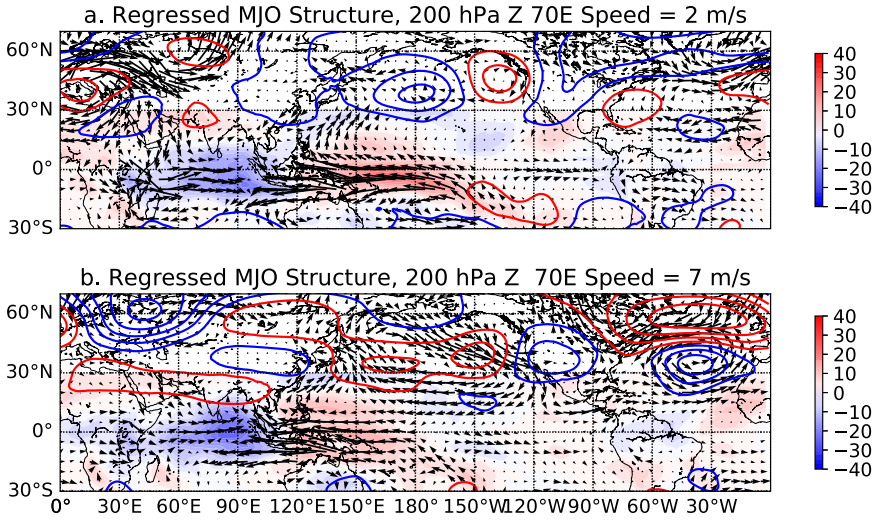

FIG. 1. Regressed shaded OLR (W m^{-2}), 850-hPa wind vector, and contoured 200-hPa geopotential height anomalies against the wavelet-filtered indices at base longitude 70°E at lag zero. The upper-tropospheric height anomalies serve for comparison against Roundy (2021). (a) Regressed against wavenumber 2 OLR anomalies at 2 m s^{-1}. (b) As in (a), but for 7 m s^{-1}. Contours are at every 10 m, with red positive contours and blue negative contours. The lowest contours are at ±5 m.

near the slowest (2 m s^{-1}) and fastest (7 m s^{-1}) of that range to assess the differences in associated atmospheric circulation signals near the extremes while remaining close enough to what could be considered MJO events. The wavelet form is given by Roundy (2021):

$$w(t,x) = \frac{1}{\sqrt{f_{bx}\pi}} \times \frac{1}{\sqrt{f_{bt}\pi}} \times \cos[2\pi(f_x x - f_t t)] \times \exp\left(\frac{-x^2}{f_{bx}}\right) \times \exp\left(\frac{-t^2}{f_{bt}}\right),$$

where x represents each longitude on the grid centered at the base longitude, t represents each day along the time series centered at a base date, f_{bx} represents longitudinal Gaussian width (set to 20 000), and f_{bt} represents temporal Gaussian width (set to 2000 for fast MJO and 6000 for slow MJO). The wavenumber f_x was set to 2, the dominant zonal scale of the MJO over the Indian Ocean warm pool. The localization constraints f_{bx} and f_{bt} were reduced relative to Roundy (2021) to better isolate the wavenumber and frequency signal instead of emphasizing localization. The center frequency f_t, defined by (2), relates the frequency to phase speed c given the wavenumber f_x:

$$f_t = \frac{f_x}{2\pi R_E} \times c \times \frac{86\,400\text{s}}{\text{day}}, \qquad (2)$$

where R_E represents the equatorial radius of Earth, and the rightmost fraction in (2) converts the units of f_t to cycles per day. The wavelet-filtered indices were formulated by multiplying the wavelet and the corresponding OLR anomalies centered at the base longitude and at a base date, and then summing the results as in a dot product. To better understand the behavior of the MJO passing through the Indian Ocean warm pool, the base longitude was set at 70°E. The wavelet moves across time, so each day acts as the base date once.

Following Roundy (2021), the regression of data fields during December–February against the 2 and 7 m s^{-1} wavelet-filtered indices characterizes the correlation of data fields with the MJO at different phase speeds to diagnose differences between slow and fast events. The regressions were scaled to two standard deviations in the base index. Wavelet regression associates data fields with signals at a specific point in the wavenumber–frequency domain, leading to weaker amplitudes of regressed signals compared to regressions associated with signals from broader regions of the wavenumber–frequency domain. However, statistical significance can still be assessed. A broad range of frequencies and wavenumbers occurring simultaneously characterize observed MJO events, not just specific points in the spectrum, but specific points in the spectrum stand out more in different events (e.g., Roundy 2022). Thus, regressions based on such specific points in the spectrum diagnose the expected patterns for events characterized by the target patterns.

To assess how the data fields evolve locally when the slow and fast MJO signals are passing through the same base longitudes, regressions are repeated along the equator at all OLR grid points from 45° to 90°E. The given data fields were regressed at the same base longitude against the wavelet-filtered index.

Statistical significance is assessed in comparison with random chance, applying the null hypothesis that the true signal associated with the base index is zero. Following Roundy (2014), randomizing the Fourier phases of the predictor indices and repeating the analysis thousand times produce null distributions at each grid point of the regressed signals. A two-sided test with a 95% confidence level diagnoses the

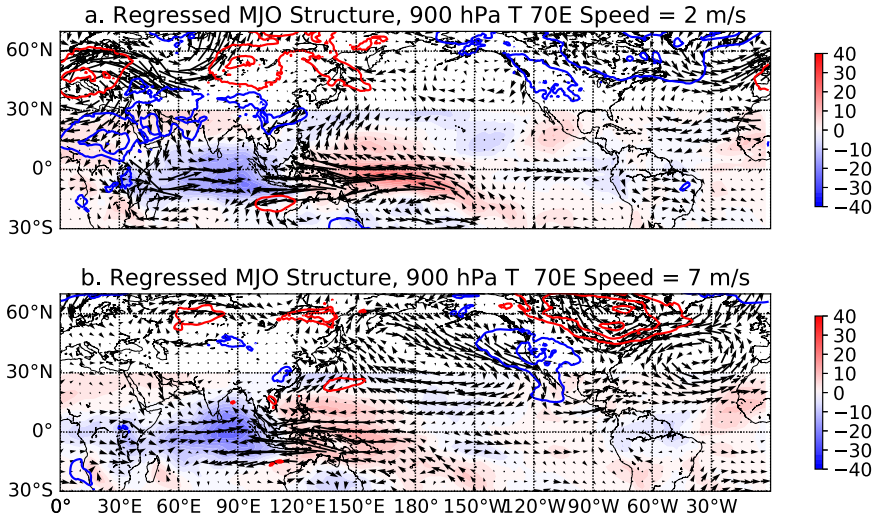

FIG. 2. As in Fig. 1, but for contours of 900-hPa temperature anomalies replacing contours of 200-hPa geopotential height anomalies at lag = 0 days. Contours are at every 0.5°C, with red positive contours and blue negative contours. The zeroth contour is omitted.

statistical significance of the difference between the regressed fields of 2 m s^{-1} MJO events and regressed fields of 7 m s^{-1} MJO events. If the regressed field falls outside the 95% confidence range of the null distribution, then we reject the null hypothesis at that grid point.

3. Results

Figures 1–3 illustrate maps of regressed data with zero time lag relative to the base indices. Each figure shows regressed shaded OLR anomalies and regressed contours of 200-hPa geopotential height (Fig. 1), 900-hPa temperature T (Fig. 2), or 850-hPa specific humidity q (Fig. 3). Vectors in all figures and panels show 850-hPa wind anomalies. Panels (a) show results for phase speed 2 m s^{-1} MJO events, and panels (b) show results for phase speed 7 m s^{-1} MJO events. Based on regressions using increased Gaussian temporal width f_{bt} (not shown here), the structures and relative amplitudes in Figs. 1–3 are not strictly sensitive to reduced time localization.

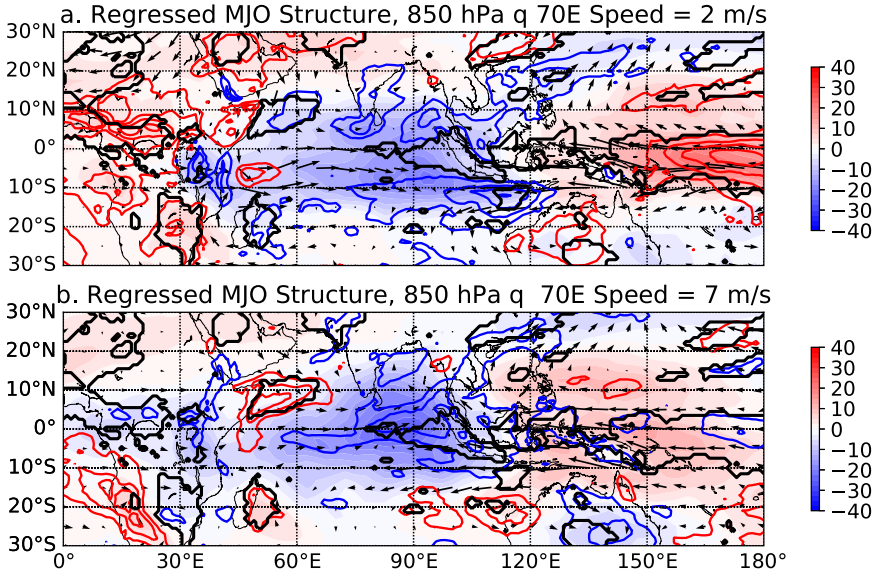

FIG. 3. As in Fig. 1, but for contours of 850-hPa specific humidity anomalies replacing contours of 200-hPa geopotential height anomalies at lag = 0 days. Contours are at every 0.002, with red negative contours and blue positive contours. The zeroth contour is omitted. The heavy black contours enclose regions where the specific humidity differences between (a) and (b) exceed the 95% confidence levels.

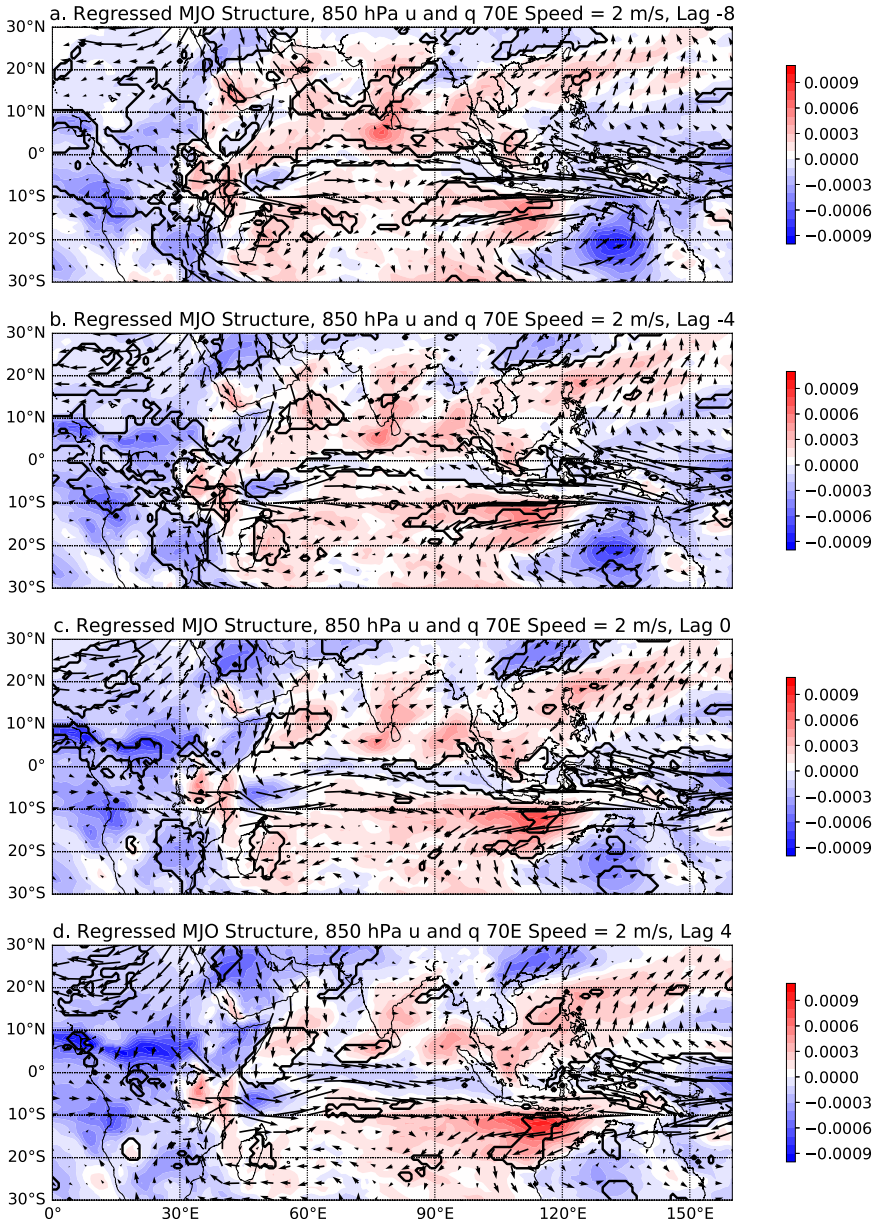

FIG. 4. Regressed 850-hPa specific humidity (shading) and wind (vectors) anomalies; as in Fig. 3a, but at time lags of the field from (a) −8 days through (d) +4 days relative to the base index. Shaded regions enclosed by dark contours indicate where the 2 m s^{-1} MJO signals are significantly drier or moister than the 7 m s^{-1} MJO signals at the 95% confidence level using the test described in section 2.

Negative OLR anomalies in Figs. 1–3 shown in blue shading suggest active convection in panels (a) and (b) over the central and eastern equatorial Indian Ocean (around 60°–90°E), consistent with the signal at the base longitude at 70°E scaled to two standard deviations to represent a strong active convective event. Negative OLR anomalies are stronger in the 7 m s^{-1} MJO regressions than in the 2 m s^{-1} MJO regressions. Regressed 850-hPa wind anomalies show westerlies to the west and easterlies to the east of the active convective region (blue shading). Looking at the wind vectors in Fig. 1a, the 2 m s^{-1} MJO westerly maximum at 1.5 m s^{-1} occurs within the negative OLR anomaly over the Indian Ocean near 5°S, 60°E. On the other hand, in Fig. 1b, the 7 m s^{-1} regression associates with weaker westerlies, maximizing near 1.25 m s^{-1} and shifting eastward to near 80°E at the equator.

Contours in Fig. 1 show 200-hPa geopotential height anomalies for comparison against the previous results of Roundy (2021). As described by Roundy (2021), the 7 m s^{-1} MJO signal features a North Atlantic blocking pattern, with a trough anomaly to the east over central and eastern Europe.

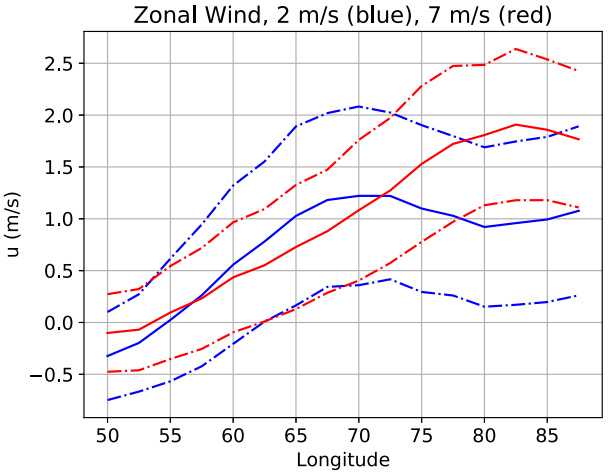

FIG. 5. Regressed equatorial zonal wind u anomalies at 850 hPa against wavelet-filtered OLR signals based at the same longitudes for 2 m s^{-1} (blue) and 7 m s^{-1} (red) MJO events. Dashed lines indicate the 95% confidence intervals.

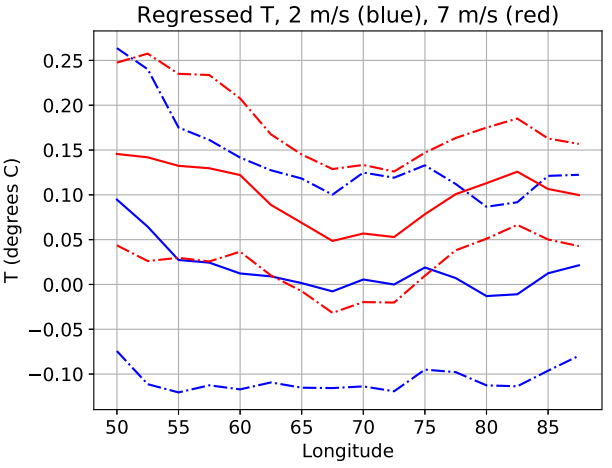

FIG. 6. As in Fig. 5, but for 850-hPa temperature T anomalies.

In Fig. 1a, the 2 m s^{-1} MJO regression shows a Greenland trough anomaly (blue contours at 90°–30°W) and a central European ridge (red contours at 0°–30°E). The 850-hPa wind flow associated with this ridge includes northerlies over North Africa and Arabia (around 30°–45°E). These results compare well with previous studies on MJO composites. Yadav and Straus (2017) show a similar European ridge at 500 hPa in their real-time multivariate MJO (RMM) index composites for slow events (see their Fig. 9, panels labeled phases 2 and 3). Figure 1a of Zheng and Chang (2019) shows composite of 500-hPa height anomalies from ERA-Interim reanalysis during RMM phase 3 with zero lag, which follows the same RMM phase with this paper's base point at 70°E. Their results show a trough over western Asia, ridge over tropical southern Asia, ridge over the northwest Pacific Ocean, trough over western North America, and ridge over the northeastern Atlantic Ocean, which matches well with Fig. 1b. The northerly wind anomalies in Fig. 2a over North Africa and Arabia coincide with a negative 900-hPa temperature anomaly (blue contours over 30°–60°E). Furthermore, another region of equatorward flow in the Southern Hemisphere is present near southeastern Africa. In contrast, Fig. 2b shows that the fast MJO excludes any substantial temperature anomalies near the active convection over the Indian Ocean.

The temperature anomalies over Africa coincide with equatorward flow and equatorial westerly anomalies over the Indian Ocean. Associated specific humidity anomalies are shown in Fig. 3. In the slow event shown in Fig. 3a, 850-hPa moist anomalies (blue contours at 60°–100°E) concentrate north and south of the equator in the gyre regions, with a region of relative dryness on the equator. The central and eastern equatorial Indian Ocean moisture anomalies are significantly stronger in the fast MJO signal (Fig. 3b) compared to the slow MJO signal (Fig. 3a). To assess how the relative equatorial dry signal emerges in slow MJO events, Fig. 4 repeats the regression analysis shown in Fig. 3a across a range of time lags.

Figure 4 shows a significant equatorial drying trend in the slow MJO signal from 8 days before to 4 days after the event. Differences in structure are evident when the slow moist and fast moist signals overlap, and the difference in phase speeds causes the two signals to come into and out of phase with each other as the fast signal outruns the slow one. The 7 m s^{-1} MJO signal propagates at more than 3 times the speed of the 2 m s^{-1} MJO.

Thus, looking at Fig. 4a at lag = −8 days, the eastern equatorial Indian basin is significantly drier during the slow signal than during the fast signal because the active phase in the slow event has yet to arrive. By lag = −4 days in Fig. 4b, the active phases overlap over the western and central equatorial basin, but the surge of stronger westerlies during the slow events in the same region associates with significantly lower specific humidity (near climatology instead of anomalously moist). By lag = 0 days in Fig. 4c, the two signals unify in location at the base point, but the western equatorial basin dried out already in the fast signal because of its more rapid advance. By lag = 4 days, the relatively low moisture anomalies of the northwestern Indian basin gyres significantly moisten more in the slow event than in the fast event because the fast event already advanced to its dry phase in the same region. The equatorial westerly jet feature connected to dry equatorward flow in the slow events significantly differs from the fast signal, and the equatorial drying occurs in the slow events even while the upper-tropospheric mass divergence of the event persists in the region (see corresponding upper-tropospheric winds by Roundy 2021).

Figures 5–7 show the equatorial regressions of zonal wind u, temperature T, and specific humidity q at each longitude across the Indian basin. These figures demonstrate how the given variables compare when the convection in the slow and fast signals occurs at the same longitudes across the Indian basin.

According to Fig. 5, as the 2 and 7 m s^{-1} signals advance eastward to each base longitude, the associated equatorial zonal wind anomaly becomes more westerly. This intensification of associated westerlies continues until a maximum near 82.5°E in the fast events and 70°E in the slow events. The confidence

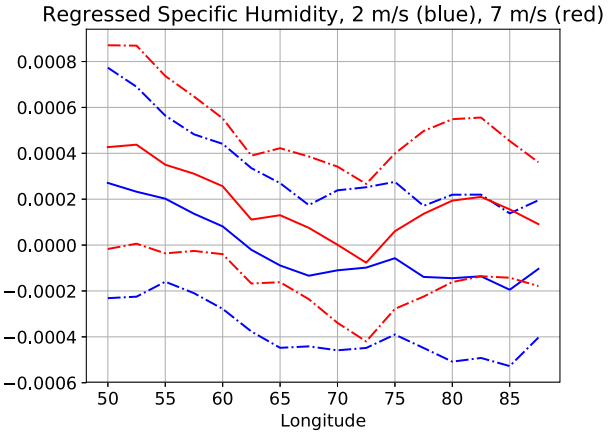

FIG. 7. As in Figs. 5 and 6, but for 850-hPa specific humidity q anomalies.

intervals (dashed lines in Fig. 5) associated with the two phase speeds overlap until the two signals reach the eastern Indian Ocean, where they become statistically distinguishable. At this point, the fast events associate with stronger westerlies, while the westerly wind intensities in the slow events level off or decline. Figures 6 and 7 also show overlapping confidence intervals for temperature and specific humidity during the slow and fast events that advance toward being distinguishable after they arrive over the eastern Indian Ocean. Positive specific humidity and temperature anomalies collocated with the center longitude of active convection tend to adjust further eastward, consistent with strengthening of the Rossby gyres and import of dry air. However, the two signals begin to separate over the eastern Indian Ocean. Temperature and specific humidity during fast events increase over the eastern basin, while temperature and specific humidity continue declining during slow events. The amplitude of westerlies in the eastern basin alone cannot explain the differences between the slow and fast events because the westerlies in the fast events continue to grow farther east becoming stronger than in the slow events. Figures 3 and 4 suggest that the westerlies in the slow events concentrate about the equator in a jet pattern, surrounded on the north and south by weaker winds a few degrees from the equator. The statistically significant separations occur with a shift to the west of the base points not shown in Figs. 5–7. To illustrate, Fig. 8 shows a regression map that replicates Fig. 7 but with regression results shifted in space from the equatorial base longitudes as well.

From Fig. 8a, the specific humidity at 67.5°E (longitude = 67.5°E) regressed against wavelet-filtered OLR 40° to the west (Longitude-Delta = −40°) has a significantly positive difference between the slow and fast MJO signals. This implies that the suppressed convection east of the approaching enhanced convection is more moist in the slow MJO event than the fast MJO event. On the other hand, the difference in regressed specific humidity at longitude = 67.5°E, Longitude-Delta = 0°, and Longitude-Delta = 40° indicates a significantly drier slow MJO signal. Thus, as the slow and fast events evolve eastward across the Indian Ocean to the Maritime Continent, the slow MJO event dries compared to the fast

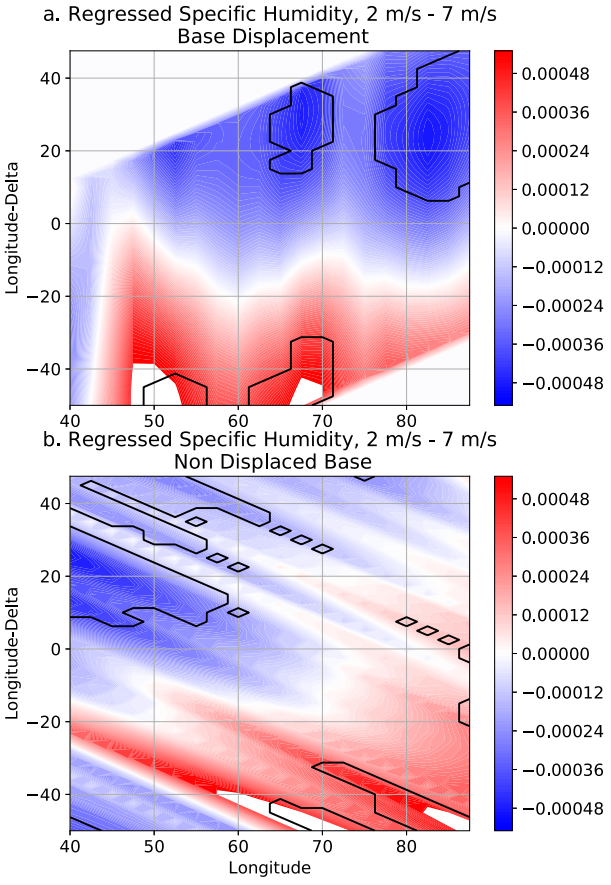

FIG. 8. Difference of the specific humidities regressed against wavelet-filtered OLR between the slow and fast MJO events (shaded) and their statistical significance (black contours). Longitude indicates the base longitude of (a) specific humidity and (b) OLR, while Longitude-Delta indicates the shift in base longitude of OLR relative to the base longitude of specific humidity.

one, and this is consistent with the relative dryness emerging from the west of the advancing convection center. Figure 8b presents the same results, but the horizontal axis indicates the base longitude of wavelet-filtered OLR and the vertical axis indicates the shift in OLR base longitude to get to the regressed specific humidity in Fig. 8a. Finally, Fig. 9 shows vertical cross sections of regressed equatorial specific humidity anomalies as a function of lead time.

Dry anomalies advance from the west in the slow events, suggesting a stratiform rain pattern beginning to mature in the slow events even before the slow and fast events collocate at the 70°E base point at lag = 0 days. The dry signal only advances in the fast events as the subsident phase more quickly arrives at lag = 4 days. Combining the above results suggest that a surge of cool dry air originating from Africa and Europe toward the Indian basin navigates along the equator with the convection over the eastern Indian basin in the slow events. Stronger eastern Indian basin westerlies occur in the fast events during increased specific humidity and temperature anomalies.

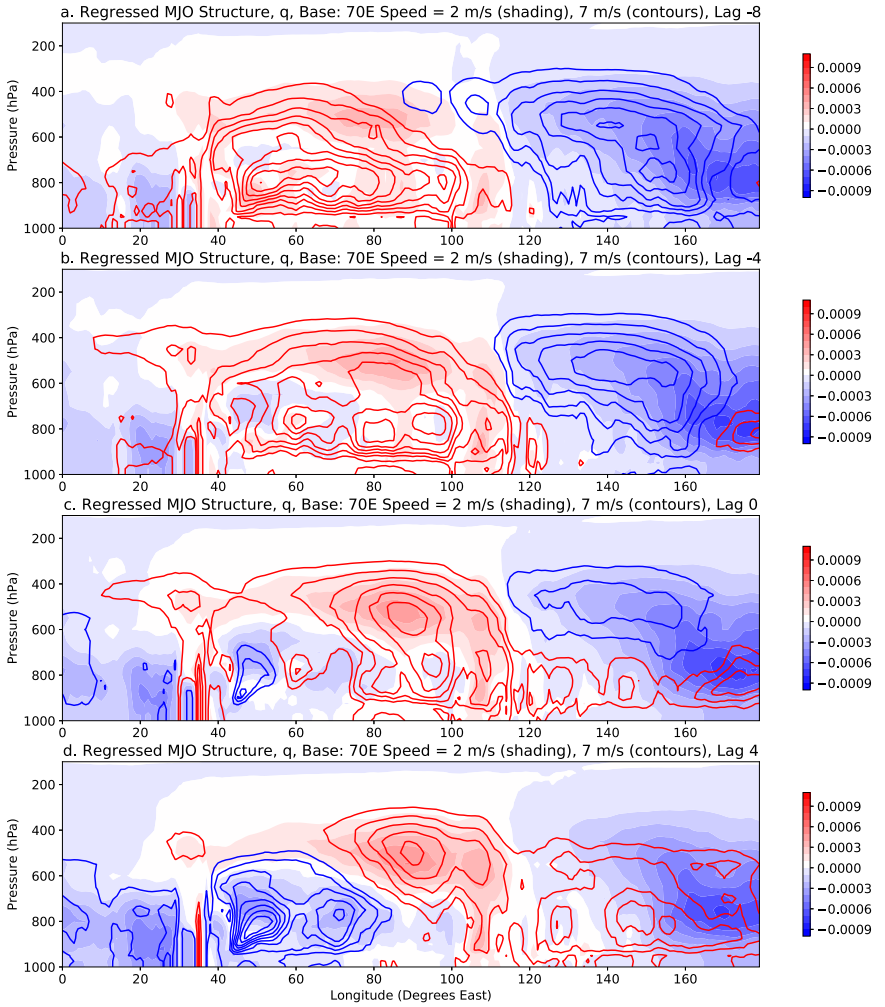

FIG. 9. Vertical cross sections of regressed specific humidity anomalies during time lags (a) −8, (b) −4, (c) 0, and (d) +4 days at base longitude 70°E. Shading represents the results for 2 m s^{-1} MJO events, while contours represent the results for 7 m s^{-1} MJO events. Positive anomalies are shown in red, and negative anomalies are shown in blue.

4. Conclusions

Previous results suggest that planetary-scale Kelvin wave features slowed down to MJO characteristic phase speeds by the upper-tropospheric background wind dominate the upper-tropospheric circulation signal associated with the MJO over the Indian Ocean. The approaching upper-tropospheric easterly wind collocates with a trough anomaly and upward motion. In situ measurements have already demonstrated that this signal approaching the basin from the west cools the deep troposphere via this anomalous upward motion, thereby increasing moist deep convection (e.g., Powell and Houze 2015). The outflow from the resultant convection does not overwhelm the original upper-tropospheric Kelvin wave trough signal (Roundy 2020). The MJO-associated upper-tropospheric circulation about the equator behaves more like a Kelvin wave over the Indian Ocean than the total MJO-associated circulation over the Western Hemisphere (Sakaeda and Roundy 2015; Roundy 2020). Arguably, the effects of moist convection dominate the lower-tropospheric circulation, which is less Kelvin wave–like.

This work extends a wavelet regression study by Roundy (2021) to assess why slowly propagating MJO events associate with weaker convection than faster events. By regressing OLR, wind, geopotential height, temperature, and specific humidity anomalies against wavelet-filtered OLR anomalies at zonal wavenumber 2 and phase speeds of 2 and 7 m s^{-1}, we showed that a surge of dry westerlies along the equator in the lower troposphere in the slow events differentiates them from the fast events. These dry westerlies trace back to cool dry air over Africa and the Middle East, sourced from a European ridge present in the slow MJO signal but absent in the fast MJO signal. The slow progress of the event allows for circulation around the tropical lower-tropospheric Rossby gyres to reach fully into the center longitudes of the deep convection along the equator. The arrival of the dry air would weaken the slow MJO convective signature and leave the strongest moisture and convective signals near the Rossby gyre cyclones

situated off the equator. This result could explain why MJO events stop intensifying with reducing phase speed in nature. A lower-tropospheric equatorial westerly jet ingests the dry air (Fig. 4), which entrains into the MJO convective envelope. Roundy (2022) demonstrated that slow MJO events experience stronger background upper-tropospheric easterlies than faster MJO events, such that the upper-tropospheric divergence associated with the slow events remains over the Indian Ocean even as the lower-tropospheric circulation entrains dry air. It is unclear from this analysis what fraction of the variance in reduced amplitude in slow MJO events can be explained by intrusion of this dry air by this mechanism. Further research, including mechanism denial experiments, may be necessary.

This result suggests a secondary hypothesis for future work that the observed MJO spectral peak may emerge in part because continents enhance the dry air intrusion into the tropics. If continents are important, we might observe weaker spectral peaks in the subseasonal range of tropical rainfall in some aquaplanet models.

Acknowledgments. Funding was provided by the National Science Foundation Grants 1757342 and 2103624 to Paul Roundy. The ECMWF provided ERA5 reanalysis data, and the NOAA ESRL provided interpolated satellite outgoing longwave radiation data.

Data availability statement. Data are freely available from the ECMWF and the NOAA ESRL. Code to replicate the analysis is available by request from the author (please give 2 weeks for response).

REFERENCES

Chen, G., and B. Wang, 2020: Circulation factors determining the propagation speed of the Madden–Julian Oscillation. *J. Climate*, **33**, 3367–3380, https://doi.org/10.1175/JCLI-D-19-0661.1.

Gill, A. E., 1980: Some simple solutions for heat-induced tropical circulation. *Quart. J. Roy. Meteor. Soc.*, **106**, 447–462, https://doi.org/10.1002/qj.49710644905.

Hendon, H. H., and M. C. Wheeler, 2008: Some space–time spectral analyses of tropical convection and planetary-scale waves. *J. Atmos. Sci.*, **65**, 2936–2948, https://doi.org/10.1175/2008JAS2675.1.

Hersbach, H., and Coauthors, 2023: ERA5 hourly data on pressure levels from 1940 to present. Copernicus Climate Change Service (C3S) Climate Data Store (CDS), accessed 31 December 2019, https://doi.org/10.24381/cds.bd0915c6.

Liebmann, B., and C. Smith, 1996: Description of a complete (interpolated) outgoing longwave radiation dataset. *Bull. Amer. Meteor. Soc.*, **77**, 1275–1277, https://doi.org/10.1175/1520-0477-77.6.1274.

Madden, R. A., and P. R. Julian, 1972: Description of global-scale circulation cells in the Tropics with a 40–50 day period. *J. Atmos. Sci.*, **29**, 1109–1123, https://doi.org/10.1175/1520-0469(1972)029<1109:DOGSCC>2.0.CO;2.

Milliff, R. F., and R. A. Madden, 1996: The existence and vertical structure of fast, eastward-moving disturbances in the equatorial troposphere. *J. Atmos. Sci.*, **53**, 586–597, https://doi.org/10.1175/1520-0469(1996)053<0586:TEAVSO>2.0.CO;2.

Powell, S. W., and R. A. Houze Jr., 2015: Effect of dry large-scale vertical motions on initial MJO convective onset. *J. Geophys. Res. Atmos.*, **120**, 4783–4805, https://doi.org/10.1002/2014JD022961.

Roundy, P. E., 2008: Analysis of convectively coupled Kelvin waves in the Indian Ocean MJO. *J. Atmos. Sci.*, **65**, 1342–1359, https://doi.org/10.1175/2007JAS2345.1.

——, 2012: Observed structure of convectively coupled waves as a function of equivalent depth: Kelvin waves and the Madden–Julian Oscillation. *J. Atmos. Sci.*, **69**, 2097–2106, https://doi.org/10.1175/JAS-D-12-03.1.

——, 2014: Regression analysis of zonally narrow components of the MJO. *J. Atmos. Sci.*, **71**, 4253–4275, https://doi.org/10.1175/JAS-D-13-0288.1.

——, 2020: Interpretation of the spectrum of eastward-moving tropical convective anomalies. *Quart. J. Roy. Meteor. Soc.*, **146**, 795–806, https://doi.org/10.1002/qj.3709.

——, 2021: The association between the phase speed of the Madden–Julian Oscillation and atmospheric circulation. *The Multiscale Global Monsoon System*, C.-P. Chang et al., Eds., World Scientific Series on Asia-Pacific Weather and Climate, Vol. 11, World Scientific, 301–314.

——, 2022: Effect of advection by upper-tropospheric background zonal wind on MJO phase speed. *J. Atmos. Sci.*, **79**, 1859–1864, https://doi.org/10.1175/JAS-D-21-0298.1.

——, and W. M. Frank, 2004: A climatology of waves in the equatorial region. *J. Atmos. Sci.*, **61**, 2105–2132, https://doi.org/10.1175/1520-0469(2004)061<2105:ACOWIT>2.0.CO;2.

Sakaeda, N., and P. E. Roundy, 2015: The development of upper-tropospheric wind over the Western Hemisphere in association with MJO convective initiation. *J. Atmos. Sci.*, **72**, 3138–3160, https://doi.org/10.1175/JAS-D-14-0293.1.

Sobel, A. H., and D. Kim, 2012: The MJO-Kelvin wave transition. *Geophys. Res. Lett.*, **39**, L20808, https://doi.org/10.1029/2012GL053380.

Suematsu, T., and H. Miura, 2022: Changes in the eastward movement speed of the Madden–Julian Oscillation with fluctuation in the Walker circulation. *J. Climate*, **35**, 211–225, https://doi.org/10.1175/JCLI-D-21-0269.1.

Takasuka, D., T. Kohyama, H. Miura, and T. Suematsu, 2021: MJO initiation triggered by amplification of upper-tropospheric dry mixed Rossby-gravity waves. *Geophys. Res. Lett.*, **48**, e2021GL094239, https://doi.org/10.1029/2021GL094239.

Tulich, S. N., and G. N. Kiladis, 2021: On the regionality of moist Kelvin waves and the MJO: The critical role of the background zonal flow. *J. Adv. Model. Earth Syst.*, **13**, e2021MS002528, https://doi.org/10.1029/2021MS002528.

Wheeler, M., and G. N. Kiladis, 1999: Convectively coupled equatorial waves: Analysis of clouds and temperature in the wavenumber–frequency domain. *J. Atmos. Sci.*, **56**, 374–399, https://doi.org/10.1175/1520-0469(1999)056<0374:CCEWAO>2.0.CO;2.

Yadav, P., and D. M. Straus, 2017: Circulation response to fast and slow MJO episodes. *Mon. Wea. Rev.*, **145**, 1577–1596, https://doi.org/10.1175/MWR-D-16-0352.1.

Yang, Y.-M., and B. Wang, 2019: Improving MJO simulation by enhancing the interaction between boundary layer convergence and lower tropospheric heating. *Climate Dyn.*, **52**, 4671–4693, https://doi.org/10.1007/s00382-018-4407-9.

Zheng, C., and E. K. M. Chang, 2019: The role of MJO propagation, lifetime, and intensity on modulating the temporal evolution of the MJO extratropical response. *J. Geophys. Res. Atmos.*, **124**, 5352–5378, https://doi.org/10.1029/2019JD030258.